Manganese oxidation states repartition in a channel-like mesoporous zirconium oxide

Nelly Couzon, Laurence Bois, Clémentine Fellah, Cristian Loestean, Fernand Chassagneux, Rodica Chiriac, Francois Toche, Lhoussain Khrouz, Arnaud Brioude, Ovidiu Ersen, et al.

Manganese oxidation states repartition in a channel-like mesoporous zirconium oxide

Nelly Couzon[1], Laurence Bois[1*], Clémentine Fellah[2], Cristian Loestean[3], Fernand Chassagneux[1], Rodica Chiriac[1], François Toche[1], Lhoussain Khrouz[4], Arnaud Brioude[1], Ovidiu Ersen[6], Lucian Roiban[5]*

[1] Univ. Lyon, Université Claude Bernard Lyon 1, Laboratoire des Multimatériaux et Interfaces, UMR CNRS 5615, 69622 Villeurbanne, France

[2] Univ. Lyon, ENS de Lyon, CNRS UMR 5276, Université Claude Bernard Lyon 1, Laboratoire de Géologie de Lyon, 9 rue du Vercors, 69364 Lyon cedex 07, France

[3] National Institute for Research and Development of Isotopic and Molecular Technologies, Department Physics of Nanostructured Systems, 67-103 Donat St., RO-400293, Cluj-Napoca, Romania

[4] Univ. Lyon, ENS de Lyon, CNRS UMR 5182, Université Claude Bernard Lyon 1, Laboratoire de Chimie, F69342, Lyon, France

[5] Univ. Lyon, INSA-Lyon, Université Claude Bernard Lyon 1, MATEIS, UMR5510 CNRS, 7 avenue Jean Capelle, 69100 Villeurbanne, France

[6] Institut de Physique et Chimie des Matériaux de Strasbourg (IPCMS), UMR 7504 CNRS - Université de Strasbourg, 23 rue du Loess, BP 43, 67034 Strasbourg Cedex 2, France

*corresponding author

E-mail address: laurence.bois@univ-lyon1.fr (L. Bois), Lucian.Roiban@insa-lyon.fr

Abstract

Here, we present a mesoporous mixed manganese zirconium oxide (MnZr) synthesized by evaporation induced self-assembly (EISA) method involving a block copolymer self-assembly method. The MnZr oxide has been fully characterized by X-ray diffraction, transmission electronic microscopy, analytical electronic tomography, nitrogen adsorption/desorption isotherms, thermogravimetric analysis, X-ray photoelectron spectroscopy and electronic paramagnetic resonance. Electronic tomography analysis reveals that a mesoporous solid solution MnZr was successfully obtained by this way, with a homogeneous dispersion of Mn. X-ray diffraction, X-ray photoelectron spectroscopy, thermal analysis and electronic paramagnetic resonance inform about the manganese oxidation states present (II, III and IV) and their location within the sample.

Key words: manganese, zirconium, mesoporous, analytical electron tomography, self-assembly block copolymer

1. Introduction

The development of catalysis area during last decades has led to an increase interest in the use of transition metals as catalysts, proposing a great alternative to noble metals, being cheaper and as efficient. More specifically, the development of manganese containing mesoporous oxide is an important challenge for oxidation catalysis applications. Mesoporous materials possess interesting properties such as narrow pore size distribution, high specific surface area or high pore volume allowing an easy diffusion of guest species [1-3]. These properties make them particularly adapted for catalysis applications. Zirconia is a really attractive transition metal oxide for catalysis thanks to its outstanding properties: high corrosion resistance, high mechanical and thermal resistance and excellent oxygen mobility [4]. Thanks to these properties, ZrO_2 is commonly used as a support and solid solutions based on ZrO_2 possess high catalytic activity [5-7]. However, to improve its characteristics and catalytic efficiency, ZrO_2 doping is often developed, leading to interesting results [8].

Manganese as supported catalyst is particularly interesting because it possesses various valence states and five stable stoichiometric oxides (MnO, Mn_3O_4, Mn_2O_3, Mn_5O_8, and MnO_2) allowing a wide range of applications [8-10]. Manganese containing catalysts have received much attention for oxidation reactions such as the oxidation of carbon monoxide or benzene [11-14] or for the combustion of toluene [15]. Also, lot of studies have shown that manganese-based catalysts exhibit good NH_3-selective catalytic reduction (SCR) activity at low temperature [16], which is a promising method for the treatment of NOx [16,17]. Therefore, the development of new synthesis methods of manganese oxide supported on mesoporous zirconia is the main challenge that could lead towards new applications. Such

challenge is most important because the way of introduction of manganese during the synthesis of the mesoporous oxide supports can strongly affect the global characteristics of the final catalyst.

Manganese is known for its ability to penetrate the lattice of ZrO_2 forming thus some solid solutions $Zr_{1-x}Mn_xO$, which induces a higher lattice oxygen mobility and high reactivity [7,13,18-24]. Manganese oxides on zirconia support have been often studied in heterogeneous oxidation catalysis such as gas-phase oxidation of hydrocarbons or chloro-carbons. Mesoporous zirconia synthesis is well described [25-27], but few studies concern the synthesis of mesoporous mixed manganese zirconium oxide and the impact of manganese on the mesoporous zirconia characteristics [14,19]. Impregnation of zirconia with manganese salt was often used [14] while the one-pot evaporation induced self-assembly (EISA) method based on the evaporation of a sol containing the F127 block copolymer and a mixture of manganese chloride and zirconium oxychloride salt is rarely described [19].

Herein, a solid solution of manganese oxide in mesoporous zirconia has been synthesized by an one-pot EISA process using the evaporation of a sol containing the F127 block copolymer and a mixture of manganese acetylacetonate and zirconium oxychloride. The mesoporous texture of Mn incorporated oxide was analyzed by X-Ray Diffraction, Transmission Electron Microscopy and N_2 adsorption-desorption isotherm. Analytical electron tomography analysis was done to evaluate the manganese dispersion inside zirconia. Manganese oxidation states have been studied by thermal analysis, X-Ray photoelectron spectroscopy and Electronic paramagnetic resonance.

2. Experimental

2.1 Materials

A poly(ethylene oxide)-poly(propylene oxide)-poly(ethylene oxide) block copolymer, Pluronic F-127 ($(EO)_{106}$-$(PO)_{70}$-$(EO)_{106}$), zirconium oxychloride octahydrate, $ZrOCl_2,8H_2O$, manganese II

acetylacetonate $[CH_3CO=CHCOCH_3]_2Mn$, were all purchased from Sigma-Aldrich and used as received.

2.2 Synthesis of the mesoporous Mn-ZrO_2 sample

Mixed MnZr oxide was prepared by modifying the method of the mesoporous zirconia synthesis previously described [23]. $ZrOCl_2,8H_2O$ (1.7 g, 5.10^{-3} mole) was mixed in ethanol (10 mL) with 1 g of block copolymer F-127. Manganese salt, Mn(acetylacetonate)$_2$ (Mn(acac)$_2$), was added in Mn/Zr = 0.14 proportion to avoid any phase separation of manganese oxide. Slow evaporation step was performed until a gel was obtained. A thermal treatment was realized at 450°C during 5 h, with a heating rate of 1°C/min. Sample was named MnZr or Zr for the sample without manganese addition. Another thermal treatment was done at 600°C during 5 h to study the impact of manganese on the crystallization of zirconia. In Table 1 are summarized the synthesized samples.

2.3 Characterization

X-ray diffraction (XRD) patterns were recorded on a PANalytical Xpert Pro diffractometer (The Netherlands) equipped with a monochromator, using Cu Kα radiation (wavelength of 1.54 Å). Fullprof (FullProf.2k, Version 5.30 - Mar2012-ILL JRC) has been used for Rietveld refinement analysis on some of the XRD patterns.

Transmission Electron Microscopy (TEM) images have been performed on a Topcon instrument at 200 kV. Samples for the TEM characterization were ground and deposed directly on a copper grid coated with holey carbon film. Analytical Electron Tomography (AET) [28,29] was also used, which is an imaging mode of electron tomography [30] allowing the 3D quantification of the chemical distribution of the components in a sample [31] by recording filtered images tilted series [32]. AET was performed in Energy Filtered TEM (EFTEM) mode using a Jeol 2100F electron microscope equipped with a GATAN Tridiem

energy filter. The samples were crushed in a mortar, then dispersed in ethanol, and ultrasonicated for 10 min. A droplet of the suspension was deposited on a microscopy holey carbon grid on which previously 5 nm Au fiducial markers was added, and the grid was dried 10 min under a heating lamp. The tilt series were recorded by using the GATAN EFTEM tomography plugin of Digital Micrograph that allows the recording of several tilt series containing images with 512 x 512 pixels each. AET requires the uses of intense electron beam that can induce irreversible damages in the sample; therefore, as ZrO_2 is the matrix, to limit these damages, only the spatial distribution of Mn was followed. At each tilt angle was recorded a filtered image of 10 eV centered on the Zero Loss peak (ZL) with an exposure time of 0.07 s. Then three filtered images wide of 36 eV were recorded on the Mn L (640 eV) peak, centered on 573 eV, 600 eV and 640 eV with an exposure time of 10 s. The last image recorded was an unfiltered image recorded with an exposure time of 0.07 s. The chemical distribution in the 2D maps of the Mn was computed using the three-windows method implemented in the EFTEM-TOMOJ [32] plugin of ImageJ. A fine alignment was done on the ZL tilt series then applied on the computed chemical map of the Mn. The volume was computed using 15 algebraic reconstruction techniques (ART) implemented in TomoJ [29]. The protocol employed on the data analysis from AET is published in [33] and the 3D quantification was done using ImageJ tools [34-36] and 3D Slicer software [37].

Characterization of porosity of the samples was performed using nitrogen adsorption/desorption isotherms on a BELSORP mini (Bel Japan). Prior to analysis, degassing samples under vacuum at 100°C was performed during 4 h. The pore size distribution (d max) and mesoporous volume were calculated from the adsorption branch of the isotherms using the Barrett-Joyner-Halenda (BJH) method [38], and the surface area was determined by the Brunauer-Emmett-Teller (BET) approach [39].

Thermogravimetric analyses (TGA) with simultaneous differential thermal analysis (SDTA) signal have been realized on a TGA/SDTA 851^e Mettler Toledo apparatus. Around 20 mg of

precursors were placed inside an 150 µL alumina crucible with a pre-pierced cover. Temperature was increased from ambient up to 1200°C at 20°C/min. Air of high purity was used as reactive gas at a rate of 50 mL. min^{-1}.

Custom-build SPECS spectrometer was used for X-Ray Photoelectron Spectroscopy (XPS). The core level lines were recorded with Al anode (1486.6eV) radiation. The etching was performed with Ar ions accelerated at 1000V. For quantitative analysis of samples, the following XPS core-level lines were recorded: Zr 3d, Mn 2p, O 1s and C 1s. Charge was referenced to adventitious C 1s peak at 284.8eV. Shirley background was subtracted from the spectra and the deconvolutions were done by using Gaussian/Lorentzian line shapes.

Electron Paramagnetic Resonance (EPR) measurements were carried out using an X-band spectrometer Bruker EMX plus, double mode.

3. Results and discussion

3.1 X-ray diffraction

The X-ray diffraction patterns of the Zr-450 and MnZr-450 oxides are given in Fig. 1a, showing the formation of tetragonal zirconia (t-ZrO_2) (JCPDS 00-042-1164). Comparison between them shows that manganese addition slows down the crystallization of tetragonal ZrO_2, since the peaks of the Mn-450 sample are broader [20, 40-42]. The absence of any manganese oxide phases in the pattern of the MnZr-450 sample indicates that manganese ions are substituted or inserted in the zirconium oxide matrix [43,44]. It has been described in the literature that with concentrations of Mn below 30 at%, it is possible to obtain samples with single-phase solid solutions ($Mn_xZr_{1-x}O_{2-\delta}$) based on a ZrO_2 structure [7,45,46]. The lower oxide crystallinity induced by manganese addition can be described more precisely by comparing the crystallite size measured from the Scherrer law (Table 2). As shown in the

pattern obtained from the pure zirconia sample, a higher crystallized state is reached with a crystallite size of 9.7 nm, instead of 4.1 nm when manganese salt is added. Another expected effect of the manganese addition is the modification of the cell parameter of zirconia. In our case, we observe a small contraction of the zirconia cell size. Various cell size evolutions are reported in the literature. The zirconium substitution by manganese is sometimes related to a cell contraction. The Mn introduction in zirconia resulted in a decrease in the lattice parameter of zirconia, related to the substitution with smaller cations Mn^{3+} (ionic radius 0.66 Å) of bigger cations Zr^{4+} (ionic radius 0.84 Å) [7,43]. But, from the published works [44,47] this decrease in the lattice parameter is observed in spite of the substitution of Zr^{4+} ions by larger Mn^{2+} ions (Mn^{2+}, radius ionic 0.93 Å), because of the increasing proportion of oxygen vacancies in the lattice. Thus, the cell expansion is explained either by the Mn^{2+} substitution or by the insertion of small Mn^{4+} (Mn^{4+}, radius ionic 0.53 Å) in the zirconia. In the work of Fanelli et al. [20], at 5% Mn, a cell expansion was evidenced which is no more observed for 30% Mn. This down-shift of the tetragonal t-ZrO_2 lines agrees with the substitution of Zr^{4+} by larger, Mn^{2+} ions. The lack of this shift in the 30% Mn was related to the competitive effect of smaller ions, mainly Mn^{3+}. In our case, the Rietveld refinement, done by supposing the zirconium substitution with manganese (Table 3), shows that the parameters *a* and *b* of the tetragonal cell are slightly smaller than those of zirconia but the *c* parameter is much smaller. The cell volume (66.45 +/- 0.05. 10^6 pm^3) is slightly smaller (69.83. 10^6 pm^3). This analysis also reveals the existence of oxygen vacancies (95.4% of anionic sites are occupied with oxygen anions) which means that an important part of manganese ions substituted to zirconium are in the Mn II state (75% if there is a mixture Mn II-Mn IV and 50% if there is a mixture Mn II and Mn III).

The X-ray diffraction patterns after a thermal treatment at 600°C are presented in Fig. 1b. In the pure zirconia sample, Zr-600, the monoclinic zirconia crystallization was evidenced, while the mixed MnZr-600 oxide was still under the tetragonal zirconia form. The addition of

Mn improves the stabilization of the zirconia in the tetragonal crystalline phase [21], without any clear evolution between 450°C and 600°C.

3.2 Transmission electron microscopy and Analytical electron tomography of MnZr sample

The MnZr samples general morphology was firstly observed by classical TEM (Fig. 2). The oxide mesostructure of MnZr-450 is clearly observed, with parallel channels of diameter 5 nm (Fig. 2a). HR TEM images show that MnZr-450 sample is constituted by crystallites of 4-6 nm size of tetragonal zirconia with d_{101} equal to 0.30 nm (Fig. 2b). Scarce crystallites of monoclinic zirconia can be also observed with d_{001}= 0.50 nm.

The TEM images of the MnZr sample treated at 600°C (Fig. 2c) show no major evolution: the oxide mesostructure and the channels of 5 nm are still clearly visible and HR TEM image shows that the MnZr-600 sample is constituted by crystallites of 4-6 nm size having mainly tetragonal zirconia. The presence of few crystallites of monoclinic zirconia can be also detected (Fig. 2d).

Analytical Electron Tomography (AET) analysis has been done only on the MnZr-450 sample. Within the estimated spatial resolutions in the mean density reconstruction (calculated from the ZL tilt series) and in the chemical selective one (deduced from the Mn 2D maps) which are 3 and 7 nm respectively, the localization of manganese inside zirconia grain seems to be quite homogenous and any segregation effect cannot be observed at the grain level (Fig. 3). In Fig. 3a is showed the EELS spectrum recorded on the analyzed sample. The position of the energy windows are showed by the black rectangles. In insert are showed the Pre-edge1, Pre-edge2 and Post-edge energy windows recorded at 0° tilt used to compute the Mn chemical map. The initial ZL projection at 0° tilt is shown (Fig 3b), followed by a typical slice extracted from the mean density volume (Fig. 3c), the corresponding slices

through the Mn chemical volume (Fig. 3d) and through the "combined" volume obtained by superposing the morphological (in red) and chemical volumic information (in green) (Fig. 3e). By analyzing this last image, we can unambiguously conclude on the homogeneity of the Mn distribution within the zirconia grain at the nanometer scale. Finally, Fig. 3f illustrates the 3D model of the analyzed grain with in insert the pores size distribution. The analysis of the ZL volume confirms the channel like structure of the pores for which the tortuosity, representing the ratio between the estimated length of the pores and the Euclidian length between the edges of the pores, is estimated at an average of 1.32±0.53. However, the analysis of the 3D data shows also that the mesoporous structure is not very well ordered at long range and can be characterized by a lot of defects regarding the spatial arrangement and orientation of the pores, in agreement with the structural disorder induced by the Mn insertion in the zirconia structure. From a quantitative point of view, this analysis allowed us also to calculate that the pores volume which represents 21% of the total volume of the grain.

3.3 Nitrogen adsorption/desorption isotherms

Textural characterizations were done using nitrogen adsorption/desorption isotherms (Table 4 and Fig. 4) on Zr-450 and MnZr-450. Specific surface area of MnZr-450 sample is 107 $m^2.g^{-1}$ and 67 $m^2.g^{-1}$ for Zr-450. The specific surface area of the mixed oxide is higher than the simple oxide [43]. The hysteresis loop indicated the presence of mesopores for both samples (Fig. 4). The pore size distribution calculated by Barret-Joyner-Halenda (BJH) from the adsorption branch showed that the mean pore diameter was around 5 nm for both samples and the mesoporous volume was equal to 0.10 cm^3/g for MnZr-450 and 0.08 cm^3/g for Zr-450. Mesoporosity is therefore improved by the presence of Mn species, even if the pores size remains unchanged. Porosities of the MnZr-450 sample, deduced from nitrogen

adsorption experiments, is around 34%, higher than the porosity deduced from analytical electronic tomography. This difference is explained by the fact that nitrogen adsorption allows to measure both inter and intra-particle porosity whereas analytic electron tomography gives intra particle porosity and has, in addition, a quite limited spatial resolution in the present case which doesn't allow to consider the smaller pores in the quantification procedure.

3.4 Thermal analysis of MnZr sample

The thermal treatment temperatures (450 °C and 600 °C) have been chosen according to the TGA/SDTA analyses, which were done under air (Fig. 5). To understand the signification of the obtained TGA and SDTA curves, we have considered a reference MnO_2 sample. The MnO_2 TGA (Fig. 5a) curve revealed a weight loss at around 400°C, attributed to the reduction of MnO_2 into Mn_2O_3 and another weight loss, at around 900°C, related to the subsequent endothermic reduction of Mn_2O_3 to α-Mn_3O_4. Two endothermic peaks can be observed at 430°C and 890°C (Fig. 5b), which correspond to the reduction of Mn IV into Mn III species and Mn III into Mn II species, as described previously.

The TGA curve of the Zr-450 sample (Fig. 5c), shows a 2% mass loss between 600°C and 1000°C. This small weight loss occurred during the crystallization of the monoclinic zirconia and corresponds to the small exothermic peak observed on SDTA signal at 600°C (Fig. 5d).

The TGA of the MnZr-450 oxide (Fig. 5e) shows a small and sharp weight loss (0.3 %) at 500°C followed by a second weight loss (1.4 %) between 600°C and 1000°C. The first weight loss is associated to the endothermic peak at 500°C, followed by a strong exothermic peak at 560°C on SDTA curve (Fig. 5f). Then, we can make the hypothesis that Mn IV inside zirconia is reduced into Mn III with some delay (compared to simple MnO_2), since the endothermic peak happens at 500°C instead of 430°C in a simple manganese oxide. The endothermic peak is

followed immediately by an exothermic peak, which could be explained by some residual carbon oxidation. Around 800°C, the noted 1.4 % weight loss is associated to a small exothermic peak, which can be related to the crystallization of monoclinic zirconia. At the end of the experiment, ZrO_2 monoclinic and Mn_3O_4 are clearly observed by X-ray diffraction on the TGA residue (not shown here).

3.5 X-ray Photoelectron Spectroscopy characterization

XPS spectrum of the MnZr-600 sample is shown in Fig. 6. The peaks at 641, 532, 436, 346 and 182 eV correspond to the binding energies of Mn 2p, O 1s, Zr 3s, Zr 3p and Zr 3d, respectively.

The $Mn2p_{3/2}$ spectra of the MnZr-600 sample at different sputtering times are shown in Fig. 7. MnO, Mn_2O_3 and MnO_2 possess respectively a Mn $2p_{3/2}$ binding energy in the range of 640.6-641.7eV, 641.7-641.9eV and 641.9-642.6 eV [7,1]. All oxidation states are observed as highlighted by the vertical lines at 641.9 eV for Mn^{4+}/Mn^{3+} and 640.6eV for Mn^{2+}. At the surface of the sample mainly Mn^{4+}/Mn^{3+} oxidation states are present. Mn^{2+} increases by depth, however the ratio is low considering that the specific “shake-up” satellite (~647 eV) is weak [7,48].

The Zr 3d spectra for sample MnZr-600 at different sputtering times are shown in Fig. 8. The spectra are deconvoluted with only one specific doublet. The observed Zr $3d_{5/2}$ binding energies are presented in Table 5, and from 181.8 to 182.1 eV correspond to Zr^{4+} oxidation state [7,48].

The quantitative analysis of the XPS spectra at different sputtering time (or different etching depth) allows the evaluation of the Mn/Zr ratio. For MnZr-600 sample (Table 5) the

Mn/Zr ratio is almost constant at 0.16. It confirms that the manganese repartition inside zirconia is homogeneous.

3.6 Electron Paramagnetic Resonance

Acquisitions in perpendicular mode of the MnZr-450 sample (Fig. 9a) showed a main signal at g=2 characteristic of the Mn II presence in an isolated or aggregated form [40]. The small signal at g=4 may be due to the presence of Mn II species with different distortion or minor Mn IV species. The parallel mode (Fig. 9b) gave other information. A small signal at g=8 was due to the presence of some Mn III species [41,45]. This analysis indicates the presence of Mn III. A strong signal at g=4 may be attributed to different Mn III species. From the EPR analysis, dissolved manganese species inside zirconia were in the possible forms Mn II, Mn III species and probably also in Mn IV.

4. Discussion

By using the EISA process, a solid solution of zirconium and manganese oxide was obtained characterized by a well-defined mesoporous texture. Within the spatial resolution estimated to few nanometers, the analytical electron tomography shows a homogeneous repartition of manganese species in the zirconium oxide grains and allows to estimate the intra-particle porosity to 21%. A higher porosity (34%) is measured by nitrogen adsorption which is due to the slight difference in the size of the pores the two analyses may take into account and also to the fact that AET provides only intra-particle porosity. The tortuosity measured by AET is quite low and this is coherent with the channel-like morphology observed by TEM, but the texture is characterized by the presence of lots of defects in the arrangement and orientations of the pores (Fig. 2a & 2c). EPR shows that Mn III and Mn II were present and probably Mn IV. XPS, in agreement with EPR, shows that manganese is present under II, III and IV states. The states III and IV, observed before etching, are present

at / or near the crystallites surface. XPS reveals that manganese is mostly under the Mn II inside the crystallites, since this state is very clearly observed state after the etching process. From XRD data, the tetragonal form of zirconia was stabilized by manganese addition. Indeed, the consequence of the manganese presence is a delay in the growth of the crystallites with increasing temperature. Then, at 600°C, the crystallite size is maintained at a value of 5 nm, corresponding to the thermodynamic field of existence of the quadratic phase [49]. The Rietveld analysis also confirms that the Mn II state is preponderant. Then, in our case, XPS and Rietveld analyses support Nandy *et al.* [46] and Valigi *et al.* [43] hypothesis that Zr IV is substituted by Mn in II oxidation state which induces the presence of oxygen vacancies to equilibrate the charge. The small change of the cell size in the solid solution MnZr-450 oxide is due to competitive effects of the Mn II substitution on one hand, and the presence of oxygen vacancies on the other hand [43]. From the thermal analysis, the experimental weight loss (0.3 %) is coherent with an equal repartition between Mn II, Mn III and Mn IV. Indeed, the reduction of Mn IV (30% of the complete Mn) into Mn III induces a calculated weight loss limited to 0.28 wt%.

The crystallization of monoclinic zirconia is delayed from 600°C to 800°C by the presence of manganese. At 1000°C, XRD analysis reveals the presence of haussmanite Mn_3O_4 and monoclinic zirconia. Since the Mn II/Mn III ratio is higher to the one necessary for the Mn_3O_4 formation, a significant part of Mn II may still be inside the monoclinic zirconia. Such substitution inside monoclinic zirconia has already been observed [47]. All these results show that manganese ions are uniformly incorporated in the frameworks of the mesoporous zirconia.

5. Conclusion

A reaction involving manganese and zirconium salts using a block copolymer in an EISA process has been used to synthesize a mixed mesoporous manganese zirconium oxide. This

mixed mesoporous oxide was studied by XRD, TEM, electron tomography, nitrogen adsorption, electron paramagnetic resonance, XPS and thermal analysis. A channel-like mesoporous oxide has been obtained with an intraparticular porosity of 21%, pores size of 5 nm and a tortuosity of 1.32. Manganese oxide was not observed as separate phase and was forming a solid solution with zirconia, which decreased zirconia crystallinity. Analytical electron tomography has shown that a homogeneous repartition at nanometric scale of the manganese was found in zirconia. EPR, TGA and XPS show that Mn II, III and IV are present in such solid solution. More specifically, XPS reveals that Mn II is mostly present in the core of crystallites while Mn III and IV are on the surface. All these results show that the partial substitution of zirconium with manganese II inside zirconia allows to maintain the tetragonal form and from this fact the textural characteristics up to 600°C. This stability opens the way towards catalytic applications of such a solid solution.

Acknowledgments

This work has been supported at the Laboratory of Multimaterials and Interfaces - UMR 5615. This work was financially supported by the Région Rhône-Alpes. The authors gratefully acknowledge Florian Molton and Carole Duboc, GHMFL-LCMI, Université Joseph Fourier Grenoble 1, for their help during the EPR experiments and the national EPR network TGE RENARD, FR 3443 – CNRS. The authors gratefully acknowledge the national EPR federation RENARD (IT CNRS 3443) and the Département de Chimie Moléculaire, Université Grenoble Alpes. LB and LR thank to the METSA (FR CNRS 3507) network for the financial support of the AET experiments.

Notes and references

[1] Y. Wang, H. Arandiyan, J. Scott, A. Bagheri, H. Dai, R. Amal, Recent advances in ordered meso/macroporous metal oxides for heterogeneous catalysis: a review, J. Mater. Chem. A, 5 (2017) 8825.

[2] L. Zhang, L. Jin, B. Liu, J. He, Templated Growth of Crystalline Mesoporous Materials: From Soft/Hard Templates to Colloidal Templates, Frontiers in Chem. 7 (2019) https://doi.org/10.3389/fchem.2019.00022.

[3] A. Taguchi, F. Schüth, Ordered mesoporous materials in catalysis, Microporous and Mesoporous Materials 77 (2005) 1–45. https://doi.org/10.1016/j.micromeso.2004.06.030.

[4] T. Tsoncheva, L. Ivanova, D. Paneva, I. Mitov, C. Minchev, M. Fröba, Cobalt and iron oxide modified mesoporous zirconia: Preparation, characterization and catalytic behaviour in methanol conversion, Microporous & Mesoporous Materials, 120 (2009) 389-396.

[5] K. Tanabe, Surface and catalytic properties of ZrO2, Materials Chemistry and Physics, 13 (1985) 347-364.

[6] J. Zippel, M. Lorenz, J. Lenzner, M. Grundmann, T. Hammer, A. Jacquot, H. Bottner, Electrical transport and optical emission of MnxZr1−xO2(0≤x≤0.5)thin films, J. of Applied Phys. 110, (2011) 043706

[7] O. A. Bulavchenko, Z. S. Vinokurov, T. N. Afonasenko, P. G. Tsyrul'nikov, S. V. Tsybulya, A. A. Saraev V. V. Kaichev, Reduction of mixed Mn–Zr oxides: in situ XPS and XRD studies, Dalton Trans., 44 (2015), 15499

[8] E. Moharreri, W. A. Hines, S. Biswas, D.M. Perry, H. Junkai D. Murray-Simmons, S.L. Suib, Comprehensive Magnetic Study of Nanostructured Mesoporous Manganese Oxide Materials and Implications for Catalytic Behavior, Chemistry of Materials. 30, (2018) 3, 1164-1177.

[9] W. Wei, X. Cui, W. Chen, D. G. Ivey, Manganese oxide-based materials as electrochemical supercapacitor electrodes, Chem. Soc. Rev. 40 (2011) 1697-1721.

[10] D. R. Miller, S. A. Akbar, P. A. Morris, Nanoscale metal oxide-based heterojunctions for gas sensing: A review, Sensors and Actuators B 204 (2014) 250-272.

[11] A. Chen, T. Miyao, K. Higashiyama, M. Watanabe, High catalytic performance of mesoporous zirconia supported nickel catalysts for selective CO methanation, Catalysis Sci. & Tech. 4 (2014) 2508-2511.

[12] S. Biswas, B. Dutta, A. Mannodi-Kanakkithodi, R. Clarke, R. W. Song, R. Ramprasad, S.L. Suib, Heterogeneous mesoporous manganese/cobalt oxide catalysts for selective oxidation of 5-hydroxymethylfurfural to 2,5-diformylfuran, Chemical Comm. 53 (2017) 86, 11751-11754.

[13] T. N. Afonasenko, , O. A. Bulavchenko, T. I. Gulyaeva, S. V. Tsybuly P. G. Tsyrulnikov; Effect of the calcination temperature and composition of the MnO_x-ZrO_2 system on its structure and catalytic properties in a reaction of carbon monoxide oxidation, Kinetics and Catalysis, 59 (2018) 1, 1046111

[14] C. Lee, Y.-. Shul, H. Einaga, Silver and manganese oxide catalysts supported on mesoporous ZrO2 nanofiber mats for catalytic removal of benzene and diesel soot, Catalysis Today, 281 (2017) 460-466

[15] Z. Hou, J. Feng, T. Lin, H. Zhang, X. Zhou, Y. Chen, The performance of manganese-based catalysts with Ce0.65Zr0.35O2 as support for catalytic oxidation of toluene, Applied Surface Science 434 (2018) 82–90

[16] J. Gao, Y. Han, J. Mu, S. Wu, F. Tan, Y. Shi, X. Li, 2D, 3D mesostructured silicas templated mesoporous manganese dioxide for selective catalytic reduction of NOx with NH3, J. Coll. & Interf. Sci., 516 (2018) 254–262

[17] B. Jia, J. Guo, H. Luo, S. Shu, N. Fang, J. Li, Study of NO removal and resistance to SO_2 and H_2O of MnOx/TiO_2, MnO_x/ZrO_2 and MnO_x/ZrO_2–TiO_2, Applied Catalysis A, General 553 (2018) 82–90

[18] J. I. Gutierrez-Ortiz, B. de Rivas, R. Lopez-Fonseca, S. Martın, J. R. Gonzalez-Velasco, Structure of Mn-Zr mixed oxides catalysts and their catalytic performance in the gas-phase oxidation of chlorocarbons, Chemosphere 68 (2007) 1004–1012

[19] Z. Miao, H. Zhao, J. Yang, J. Zhao, H. Song, L. Chou, Mesoporous Mn–Zr composite oxides with a crystalline wall: synthesis, characterization and application, Dalton Trans., 44 (2015) 2997

[20] E. Fanelli, M. Turco, A. Russo, G. Bagnasco, S. Marchese, P. Pernice, A. Aronne, MnO_x /ZrO_2 gel-derived materials for hydrogen peroxide decomposition, J Sol-Gel Sci Technol. 60, (2011) 426-436

[21] M.L. Hernandez, J.A. Montoya, P. Del Angel, I. Hernandez, G. Espinosa, M.E. Llanos, Influence of the synthesis method on the nanostructure and reactivity of mesoporous Pt/Mn-WO_x-ZrO_2 catalysts, Catalysis Today 116 (2006) 169-178

[22] A.J. Carrillo, D. Sastre, L. Zazo, D.P. Serrano, J.M. Coronado, P. Pizarro, Hydrogen production by methane decomposition over MnOx/YSZ catalysts, Int J of Hydrogen Energy 4 1 (2016) 19382-19389.

[23] M. I. Zaki, M. A. Hasan, L. Pasupulety, Nasr E. Fouad, H. Knozinger, CO and CH4 total oxidation over manganese oxide supported on ZrO_2, TiO_2, TiO_2–Al_2O_3 and SiO_2–Al_2O_3 catalysts, New J. Chem., 23 (1999) 1197-1202.

[24] D. Döbber, D. Kießling, W. Schmitz, G. Wendt, MnO_x/ZrO_2 catalysts for the total oxidation of methane and chloromethane, Applied Catalysis B: Environmental 52 (2004) 135-143.

[25] Q. Yuan, L-L Li, S-L Lu, H-H Duan, Z-X Li, Y-X Zhu,C-H Yan, Facile synthesis of Zr-based functional materilas with highly ordered mesoporous structures, J. Phys. Chem. C 113 (2009) 4117-4124.

[26] K. Yuan, X. Jin, Z. Yu, X. Gan, X. Wang, G. Zhang, L. Zhu, D. Xu, Electrospun mesoporous zirconia ceramic fibers for catalyst supporting applications, Ceramics International 44 (2018) 282-289.

[27] D. Gu, W. Schmidt, C. Pichler, H.J Bongard, B. Spliethoff, S. Asahina, C. Shunsuke; Z. Cao, O. Terasaki, F. Schuth, Surface-Casting Synthesis of Mesoporous Zirconia with a CMK-5-Like Structure and High Surface Area, Angewandte Chemie, 4, 56, 37, (2017) 11222

[28] P. A. Midgley, R. E. Dunin-Borkowski, Electron tomography and holography in materials science, Nature Materials, 8 (2009) 271–280

[29] H. Friedrich, P. E. de Jongh, A. J. Verkleij, K. P. de Jong, Electron tomography for heterogeneous catalysts and related nanostructured materials, Chem. Rev., 2009, 109, 5, 1613-16629.

[30] M. Weyland, P. A. Midgley, Electron tomography, Materials Today, 17, 12 (2004) 32-40.

[31] C. Messaoudi, N. Aschman, M. Cunha, T. Oikawa, C.O. Sanchez Sorzano, S. Marco, Three-Dimensional Chemical Mapping by EFTEM-TomoJ Including Improvement of SNR by PCA and ART Reconstruction of Volume by Noise Suppression, Microscopy and Microanalysis, 19, 16 (2013) 1669-16.

[32] https://www.jove.com/video/56671/obtaining-3d-chemical-maps-energy-filtered-transmission-electron

[33] L. Roiban, O. Ersen, C. Hirlimann M. Drillon, A. Chaumonnot, L. Lemaitre, A.-S. Gay, L. Sorbier, Three-Dimensional Analytical Surface Quantification of Heterogeneous Silica-Alumina Catalyst Supports, Chem.Cat. Chem 9, (2017) 3503 – 3512.

[34] M. Doube M. M. Kłosowski, I. Arganda-Carreras, Fabrice P. Cordelières, P. Dougherty, J. S. Jackson, B. Schmid, J. R. Hutchinson, S. J. Shefelbine, BoneJ: Free and extensible bone image analysis in ImageJ. Bone 47 (2010) 1076-1079

[35] E. Maire P. Colombo, J. Adrien, L. Babout, L. Biasetto, Characterisation of the morphology of porous ceramics by 3D image processing of X-ray tomography data, J. Eur. Ceram. Soc. 27, 4 (2007) 1973-1981

[36] https://imagej.nih.gov/ij/plugins/volume-viewer.html

[37] A. Fedorov, R. Beichel, J. Kalpathy-Cramer, J. Finet, J.-C. Fillion-Robin, S. Pujol, C. Bauer, D. Jennings, F. Fennessy, M. Sonka, J. Buatti, S. Aylward, J. V. Miller, S. Pieper, R. Kikinis, 3D Slicer as an image computing platform for the Quantitative Imaging Network, Magnetic Resonance Imaging, 30, 9 (2012) 1323-1341

[38] Elliott P. Barrett, Leslie G. Joyner, Paul P. Halenda, The Determination of Pore Volume and Area Distributions in Porous Substances. I. Computations from Nitrogen Isotherms, J. Am. Chem. Soc. 731,(1951) 373-380

[39] S. Brunauer, P. H. Emmet, E. Teller, Adsorption of Gases in Multimolecular Layers, J. Am. Chem. Soc., 60(2), (1938)309-319

[40] M. Ozawa, K. Hashimoto, S. Suzuki, Structural and ESR characterization of heat-stable manganese -alumina lean NO removal catalyst, Applied Surface Science, 121(1997) 437-440.

[41] B. Conlan, N. Cox, J.H. Su, W. Hillier, J. Messinger, W. Lubitz, P. Leslie Dutton, T. Wydrzynski, Photo-Catalytic oxidation of a di-nuclear manganese centre in an engineered bacterioferritin reaction centre. Biochimica & Biophysica Acta, 1787 (20009) 1112-1121.

[42] J.I. Gutierrez-Ortiz, B. de Rivas, R. Lopez-Fonseca, S. Martin, J. R. Gonzales-Velasco, Structure of Mn-Zr mixed oxides catalysts and their catalytic performance in the gas-phase oxidation of chlorocarbons, Chemosphere, 68, (2007) 1004-1012.

[43] M. Valigi, D. Gazzoli, R. Dragone, A. Marucci, G. Mattei, Manganese oxide–zirconium oxide solid solutions. An X-ray diffraction, Raman spectroscopy, thermogravimetry and magnetic study, J. Mater. Chem. 6, 1996, 403-408.

[44] L. Tao, T.A. Stich, A.V. Soldatova, B.M. Tebo, T.G Spiro, W.H. Casey, R.D. Britt, Mn(III) species formed by the multi-copper oxidase MnxG investigated by electron paramagnetic resonance spectroscopy, Journal of Biological Inorganic Chemistry, 23 7, (2018) 1093-1104.

[45] D. Pomykalska, M. M. Bućko, M. Rękas, Electrical conductivity of MnO_x-Y_2O_3-ZrO_2 solid solutions, Solid State Ionics, 181 (2010) 48-52

[46] A. Nandy, A. Dutta, S.K. Pradhan, Microstructure correlated electrical conductivity of Manganese alloyed nanocrystalline cubic zirconia synthesized by mechanical alloying, Advanced Powder Technology 28 (2017) 618-628

[47] S Pattanaik, S. Martha, M. K. Sharma, S. K. Pradhan, R. Sakthivel, R. Chatterjee, D. K. Mishra, Enhancement of room temperature ferromagnetism in nanocrystalline $Zr_{1-x}Mn_xO_2$ by the suppression of monoclinic structure of zirconia, Journal of Magnetism and Magnetic Materials 494 (2020) 165768

[48] https://xpssimplified.com/elements/manganese.php

[49] G. Sharma, S. V. Ushakov, A. Navrotsky, Size driven thermodynamic crossovers in phase stability in zirconia and hafnia, J Am Ceram Soc. 101 (2018) 31-35.

Tables

Table 1 Summary of MnZr oxide materials prepared

Sample	Molar ratio of Mn: Zr
Zr-450	0: 1
Zr-600	0: 1
MnZr-450	0.14: 1
MnZr-600	0.14: 1

Table 2 Summary of the Zr and MnZr oxide crystallite size (calculated from the (101) position and width).

Sample	2Theta	width (°)	Crystallite size (nm)
Zr-450	30.34	0.90	9.7
MnZr-450	30.42	2.11	4.1
Zr-600	30.23	0.50	17.5
MnZr-600	30.41	1.70	5.0

Table 3 Summary of the Rietveld refinement of the MnZr-450 sample

Sample	a (nm)	b (nm)	c (nm)	Occup Zr* (%)	Occup Mn* (%)	Occup O* (%)	O/(Zr+Mn)	Bragg R-Factor	RF-Factor
MnZr-450	0.3632 +/0.0001	0.3632 +/0.0001	0.5041 +/-0.0002	87.7	12.3	95.4	1.908	2.09	1.26

*OccupZr and OccupMn: cationic site occupancy rate for Zr and Mn cations.
*OccupO: anionic site occupancy rate for O anions.

Table 4 Summary of the textural properties of the MnZr oxide from nitrogen adsorption/desorption measurements.

Sample	Specific surface area (m^2/g)	Porous volume (cm^3/g)	Mesoporous volume (cm^3/g)	pore size (nm)
MnZr-450	107	0.13	0.10	5.0
Zr-450	67	0.10	0.08	4.8

Table 5: Atomic ratios of elements and binding energies (eV) observed during depth profile analysis at different sputtering times (Sp. Time) with their corresponding oxidation state according to [7], for sample MnZr-600.

Sp Time (min)	**Depth (nm)**	**Mn/Zr**	**Zr3d$_{5/2}$ (eV)**		**Mn 2p$_{3/2}$ (eV)**
			ZrO_2	**MnO**	**Mn_2O_3/MnO_2**
0	0.00	0.16	182.0	640.6	642
10	0.11	0.16	182.1	640.6	642
40	0.45	0.16	182.1	640.6	642
100	1.11	0.15	181.8	640.6	641.8
160	1.78	0.15	181.8	640.6	641.9

Figures Caption

Fig. 1. X-ray diffraction patterns of a: Zr-450 (black) and MnZr-450 (blue), b: Zr-600 (black) (blue stars point the remaining tetragonal phase) and MnZr-600 (blue).

Fig. 2. TEM (a) and HRTEM (b) images of MnZr-450 sample. TEM (c) and HRTEM (d) images of MnZr -600 sample.

Fig. 3. Analytical electron tomography: a) Recorded EELS spectrum on the analysed sample showing the position of the energy windows. In insert are showed the energy filtered projections recorded at 0° from which the Mn chemical map was computed using the three windows method. b) TEM projection of the MnZr-450 sample. c) typical cross sections through the reconstructed volume obtained from the zero loss tilt series, d) corresponding chemical Mn slice, at the same depth and orientation, e) superposition of the chemical selective slice (in green) and the mass selective one (in red) and f) 3D mode of the analysed grain with, in insert, the pore size distribution calculated from the ZL volume.

Fig. 4. N_2 adsorption-desorption isotherms and pore size distribution (BJH) curves (inserts) for a: MnZr-450 sample and b: Zr-450 sample.

Fig. 5. TGA & SDTA curves of the MnO_2 (a,b), Zr-450 (c,d) and MnZr-450 (e,f) oxides.

Fig. 6. XPS spectrum of the MnZr-600 sample.

Fig.7. XPS spectra of Mn 2p at different sputtering times (up to 1.78 nm depth), corresponding to MnZr-600 sample.

Fig. 8. XPS spectra of Zr 3d at different sputtering times (up to 1.78 nm depth), corresponding to MnZr-600 sample.

Fig. 9. EPR spectra (15 K) of the MnZr-450 sample, a: perpendicular mode and b: parallel mode.

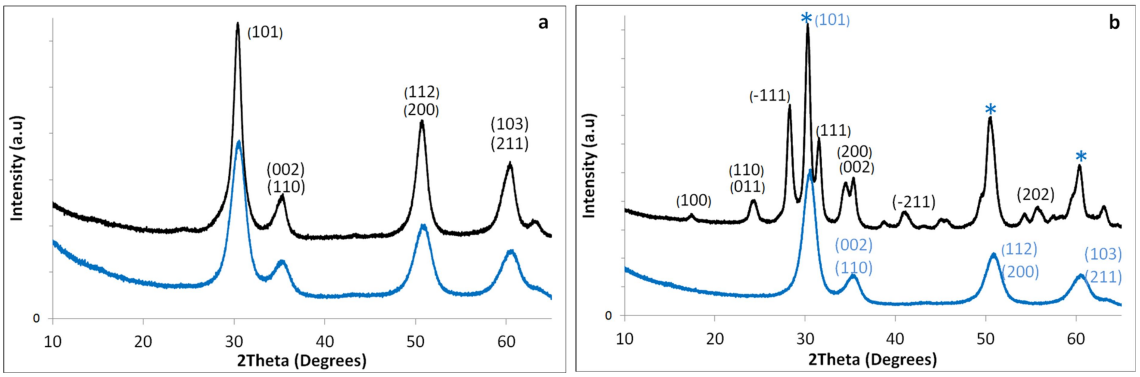
a
Intensity (a.u)
(101)
(002)
(110)
(112)
(200)
(103)
(211)
0
10
20
30
40
50
60
2Theta (Degrees)
b
Intensity (a.u)
*(101)
(-111)
(111)
(200)
(002)
(110)
(011)
(100)
(-211)
(202)
*
*
(002)
(110)
(112)
(200)
(103)
(211)
0
10
20
30
40
50
60
2Theta (Degrees)

Fig. 1.

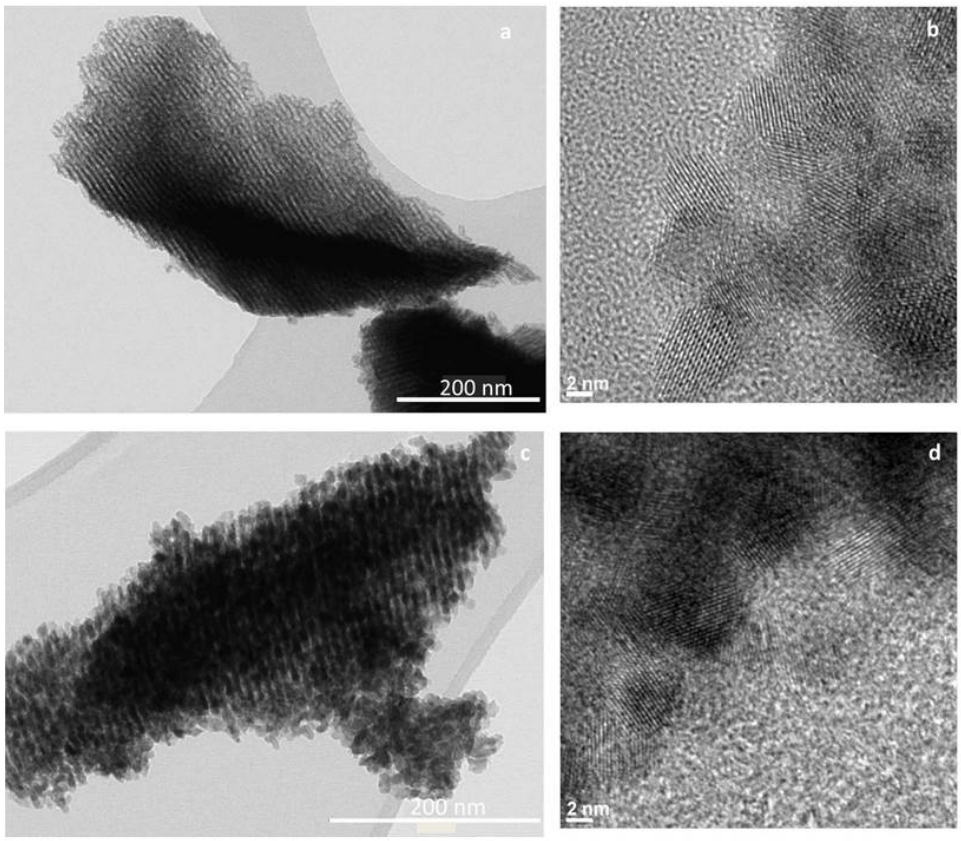

Fig. 2.

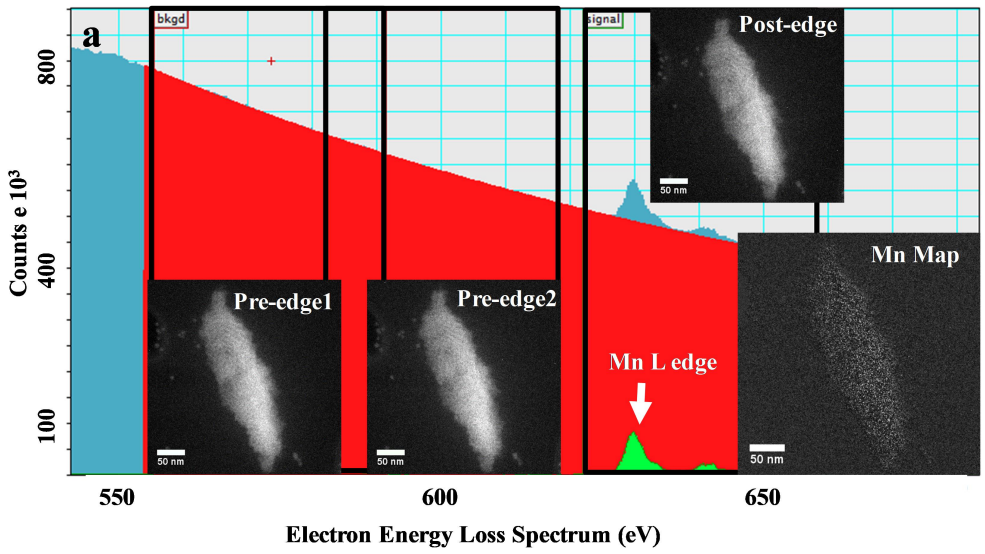

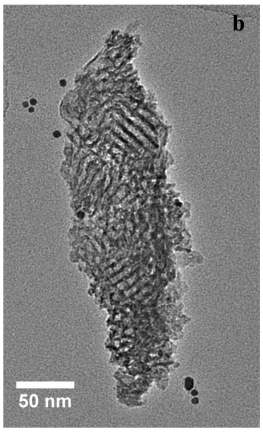

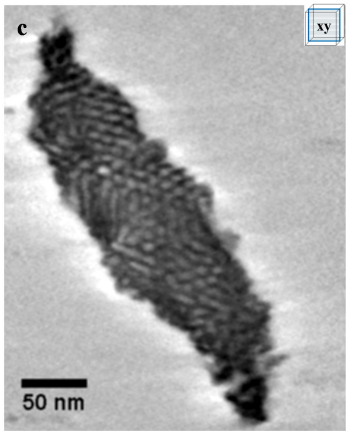

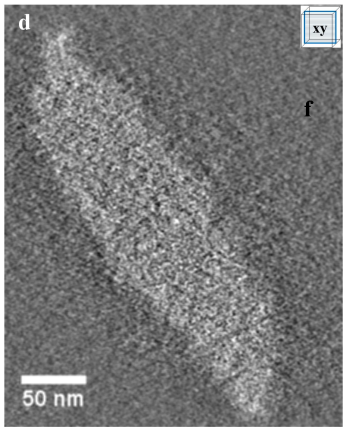

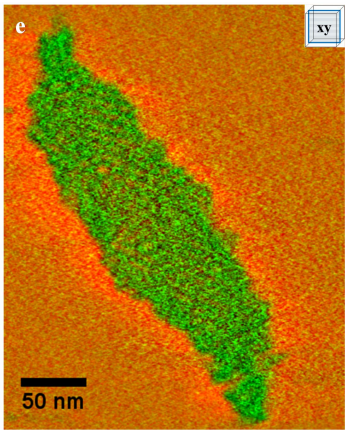

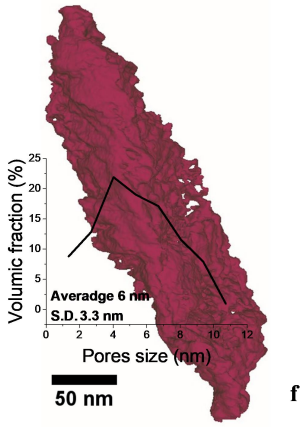

Fig. 3. Analytical electron tomography: a) Recorded EELS spectrum on the analysed sample showing the position of the energy windows. In insert are showed the energy filtered projections recorded at 0° from which the Mn chemical map was computed using the three windows method. b) TEM projection of the MnZr-450 sample. c) typical cross sections through the reconstructed volume obtained from the zero loss tilt series, d) corresponding chemical Mn slice, at the same depth and orientation, e) superposition of the chemical selective slice (in green) and the mass selective one (in red) and f) 3D mode of the analysed grain with, in insert, the pore size distribution calculated from the ZL volume.

Fig. 3.

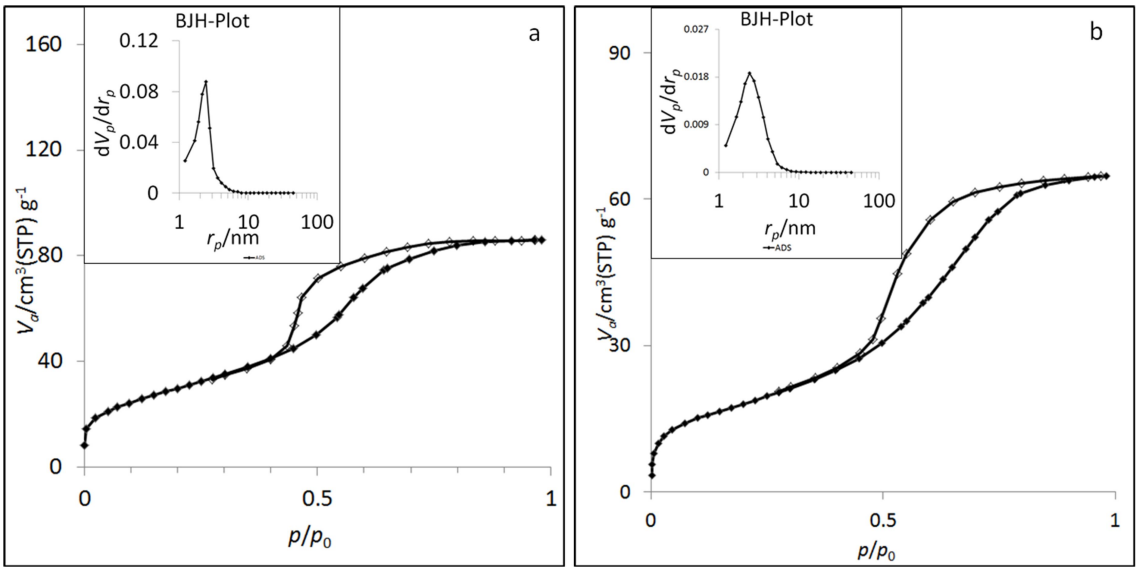
a
BJH-Plot
160
120
80
40
0
0.12
0.08
0.04
0
1
10
100
dV_p/dr_p
r_p/nm
V_a/cm^3(STP) g^{-1}
0
0.5
1
p/p_0
b
BJH-Plot
90
60
30
0
0.027
0.018
0.009
0
1
10
100
dV_p/dr_p
r_p/nm
ADS
V_a/cm^3(STP) g^{-1}
0
0.5
1
p/p_0

Fig. 4.

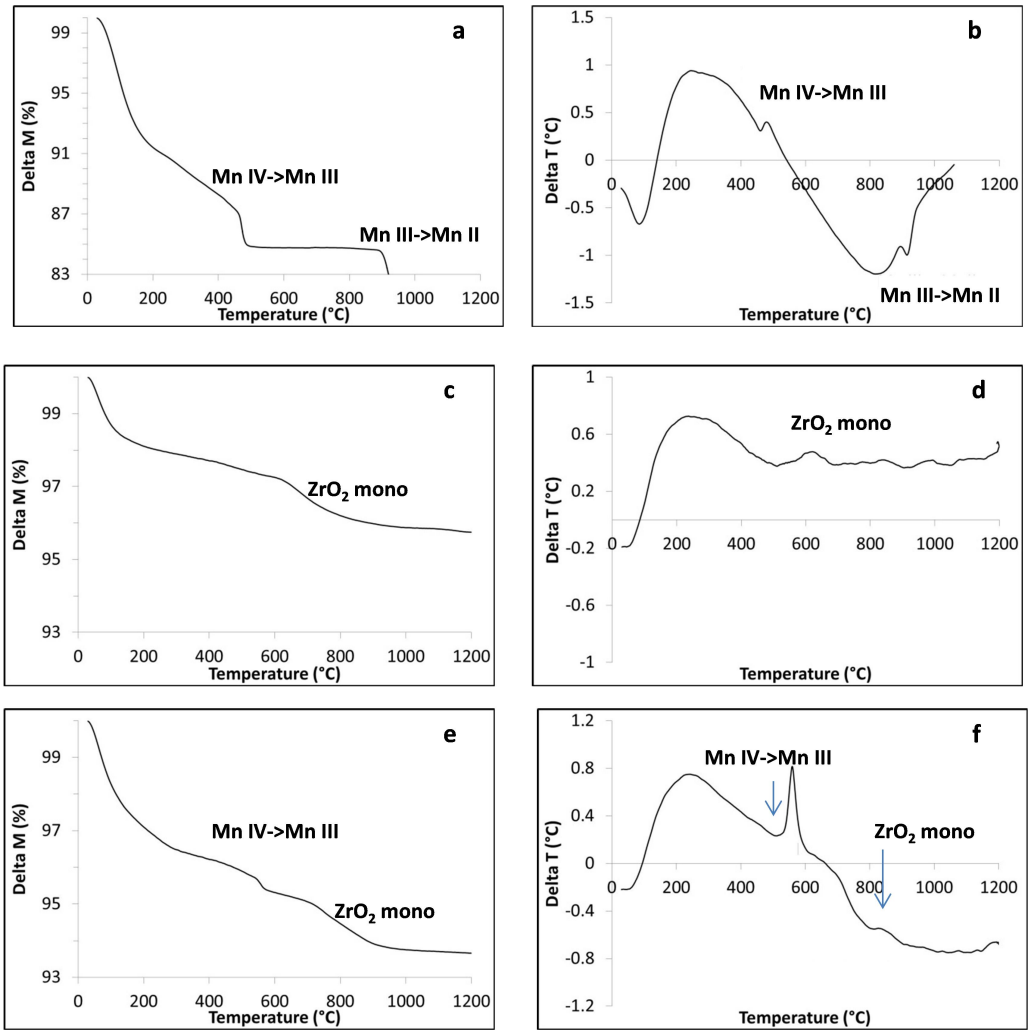
a
Delta M (%)
99
95
91
87
83
Mn IV->Mn III
Mn III->Mn II
0 200 400 600 800 1000 1200
Temperature (°C)
b
Delta T (°C)
1.5
1
0.5
0
-0.5
-1
-1.5
Mn IV->Mn III
Mn III->Mn II
0 200 400 600 800 1000 1200
Temperature (°C)
c
Delta M (%)
99
97
95
93
ZrO2 mono
0 200 400 600 800 1000 1200
Temperature (°C)
d
Delta T (°C)
1
0.6
0.2
-0.2
-0.6
-1
ZrO2 mono
0 200 400 600 800 1000 1200
Temperature (°C)
e
Delta M (%)
99
97
95
93
Mn IV->Mn III
ZrO2 mono
0 200 400 600 800 1000 1200
Temperature (°C)
f
Delta T (°C)
1.2
0.8
0.4
0
-0.4
-0.8
-1.2
Mn IV->Mn III
ZrO2 mono
0 200 400 600 800 1000 1200
Temperature (°C)

Fig. 5.

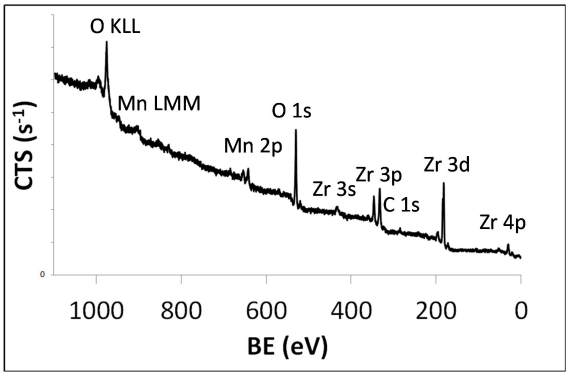
O KLL
Mn LMM
O 1s
Mn 2p
Zr 3s
Zr 3p
C 1s
Zr 3d
Zr 4p
CTS (s-1)
0
1000
800
600
400
200
0
BE (eV)

Fig. 6.

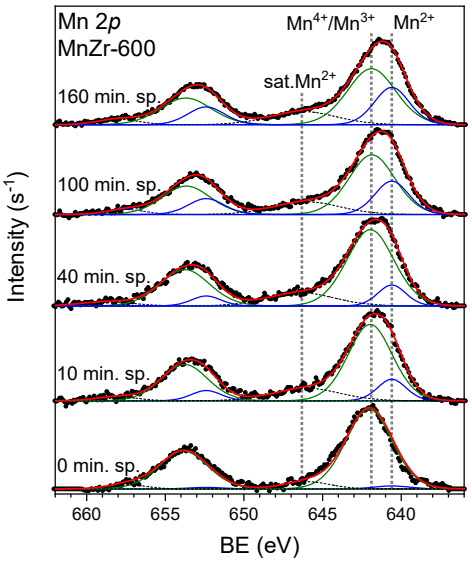

Fig.7. XPS spectra of Mn 2p at different sputtering times (up to 1.78 nm depth), corresponding to MnZr-600 sample.

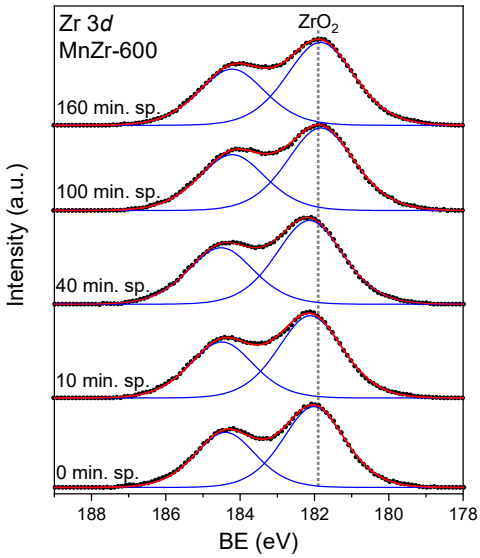

Fig. 8. XPS spectra of Zr 3d at different sputtering times (up to 1.78 nm depth), corresponding to MnZr-600 sample.

Fig. 7 & 8

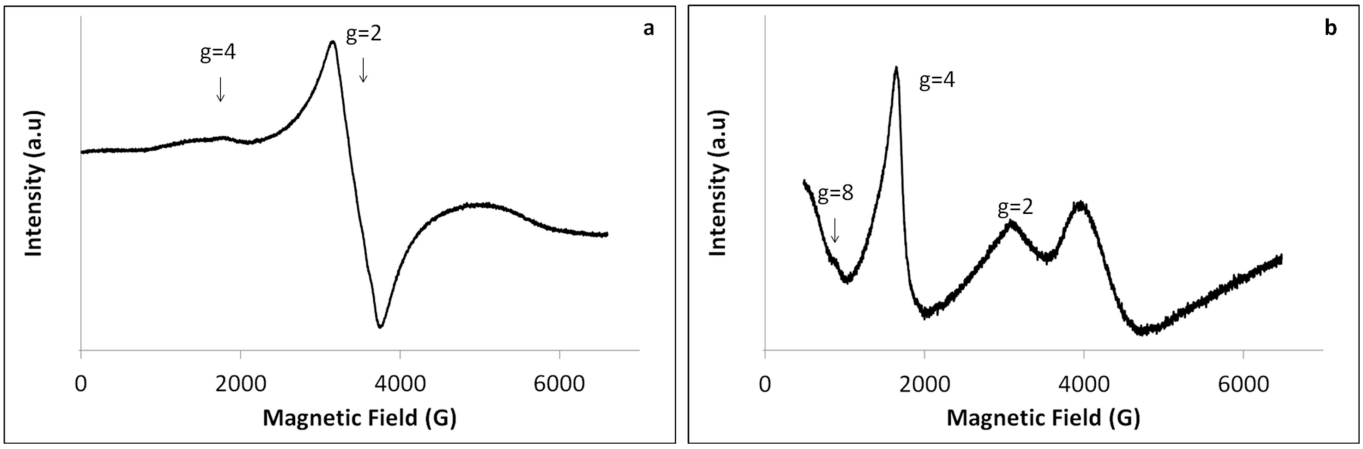
a
g=4
g=2
Intensity (a.u)
0
2000
4000
6000
Magnetic Field (G)
b
g=4
g=8
g=2
Intensity (a.u)
0
2000
4000
6000
Magnetic Field (G)

Fig. 9

Highlights

Block copolymer self-assembly process is used to form a mixed manganese and zirconium oxide

A robust mesoporous channel- like texture of MnZr oxide is obtained

Analytical Electron tomography proves that manganese is homogeneously distributed

Mn II substitutes Zr IV

Graphical abstract